Advanced Materials Science and Technology Vol 5 Issue 1 2023
DOI: 10.37155/2717–526X–0501–2

ORIGINAL RESEARCH ARTICLE

Open Access

Atomically Dispersed Co Atoms Stabilized by Nitrogen Species in Carbon Skeleton for Efficient Oxygen Reduction and Zn-air Batteries

Rongrong Liu, Jizheng Feng and Tao Meng*

College of Science, Hebei Agricultural University, Baoding 071001, China.

***Correspondence to:** Tao Meng, College of Science, Hebei Agricultural University, Baoding 071001, China. Email: taomeng@hebau.edu.cn

Received: December 22, 2022; **Accepted:** March 1, 2023; **Published Online:** March 9, 2023

Citation: Liu R, Feng J and Meng T. Atomically Dispersed Co Atoms Stabilized by Nitrogen Species in Carbon Skeleton for Efficient Oxygen Reduction and Zn-air Batteries. *Advanced Materials Science and Technology*, 2023;5(1):0511676. https://doi.org/10.37155/2717-526X-0501-2

Abstract: Atomically dispersed and nitrogen-coordinated single metal atom implanted into the carbon substrate holds great promise as Pt-liked catalysts for oxygen reduction reaction (ORR). However, the complicated synthetic procedures of single atomic catalysts heavily limit their widespread applications. Herein, the atomically dispersed Co stabilized by nitrogen species in carbon skeleton (Co-SAs/NC) is prepared by a controllable pyrolysis of the nano-confined Co-precursor, and further employed as alkaline ORR catalyst. The atomic configuration and electronic structure of Co-SAs/NC are systematic investigated by a wide range of advanced techniques, such as electron microscopic and X-ray absorption spectroscopy. As expected, Co-SAs/NC exhibites excellent ORR activity with a large onset and half-wave potentials, as well as good selectivity and favorable stability. More importantly, the outstanding ORR performances of Co-SAs/NC enable the assembled Zn-air battery to deliver a large specific capacity of 788.4 mAh•g_{Zn}^{-1}, a maximum power density of 233.6 mW•cm^{-2}, and a long cycle life.

Keywords: Atomically dispersed Co sites; Oxygen evolution reaction; Zn-air battery

1. Introduction

Metal-air batteries are promising renewable energy technologies with the advantages of high energy conversion efficiency, safety, and nontoxicity[1-3]. However, the energy conversion efficiency of metal-air batteries heavily depends on the air-cathode performances of electrocatalytic oxygen reduction reaction (ORR)[4]. The ORR generally undergoes the multiple proton-coupled electron transfer steps with complex reaction intermediates (OO*, OOH*, O*, and OH*), therefore, the catalyst with high activity are required to break down the

corresponding reaction barrier and improve the ORR activity[5,6]. Currently, the Pt-based electrocatalysts show the highest ORR activity, and are promising used for commercial applications[7,8]. However, the high-cost and scarcity of the Pt may severely hinder its large-scale applications. Thus, it is urgent to develop efficient and stable non-noble metal catalysts to replace Pt-based ones. In the past few years, carbon-based materials and transition metal compounds have been developed as efficient ORR electrocatalysts[9-11]. Among these catalysts, the hybrids of transition metal and nitrogen doped carbon (M-N-C) have been attracted much attention due to their easy availability as well as high ORR activity[12,13]. Generally, the activity origin of M-N-C catalysts is believed to be the M-N_x species[14,15]. Therefore, the key to enhance the ORR catalytic ability of M-N-C catalysts is to increase the density of M-N_x sites.

Currently, the transition metal single atoms (SAs) anchored on N-doped carbon substrates (M-N_4) with a porphyrin architecture have attracted much attention in ORR[16,17]. In comparison with transition metal nanoparticles and/or nanocrystallines, their homogeneous dispersed atomic sites enable the metal single atom catalysts (SACs) with maximum atom utilization efficiency[18,19]. Among these M-N_x SACs, atomically dispersed and nitrogen-coordinated Co atoms (Co-SACs) have been demonstrated to be the high activity ORR catalysts. Much effort has been done to increase the corresponding ORR activity by tuning the microstructure and/or electronic structure of Co-SACs[20-23]. For examples, Li group[21] reported that the Co single atoms were anchored in hierarchically porous N-doped carbon by a dual-template strategy, which is favor for exposure of the active sites and facilitating mass transfer during ORR process. Wang *et al*.[20] highlighted that the electronic density of Co single site could be regulated by designing of the corresponding atomic configuration, and the as-reported Co_1-N_3PS active moiety displayed excellent ORR activity. Although enormous progress has been made in designing high activity Co-SACs catalysts for ORR, most of the synthetic strategies for Co-SACs suffer from the expensive precursors and complex procedures, which heavily limit the widespread applications of Co-SACs. Therefore, the development of simple and efficient synthesis methods is meaningful for extensive application of single atomic catalysts.

In this work, we successfully synthesize the novel atomically dispersed and nitrogen-coordinated single-atom Co moieties implanted into the N-doped carbon (Co-SAs/NC), and investigate its ORR performance in alkaline electrolyte. Specifically, the Co-SAs/NC was prepared by a controllable pyrolysis of the Co-precursor, which was assembled by encapsulating the $Co(NO_3)_2 \cdot 6H_2O$ into the frameworks of ZIF-8 *via* a nano-confined strategy. Then, the atomic configuration and electronic structure of Co-SAs/NC were systematic investigated by the advanced techniques, such as electron microscopic and X-ray absorption spectroscopy. As expected, Co-SAs/NC exhibits excellent a large onset and half-wave ORR potentials of 1.01 V and 0.87 V, respectively, as well as good selectivity and favorable stability. And, the outstanding ORR performances of Co-SAs/NC enable the assembled Zn-air battery to deliver a large specific capacity of 788.4 mAh • g_{Zn}^{-1}, a maximum power density of 233.6 mW • cm^{-2}, and a long cycle life (1000 cycles).

2. Experimental Section

2.1 Preparation of Co-SAs/NC

There are two steps for preparation of Co-SAs/NC. Firstly, Co-ZIF-8 precursors were prepared by following step. Typically, $Zn(NO_3)_2 \cdot 6H_2O$ (3.0 g) and $Co(NO_3)_2 \cdot 6H_2O$ (0.1 g) were dispersed in water solution (50 mL) under intensive stirring. Then, another water solution (50 mL) containing of 2-methylimidazole (11.2 g) was added into above solution and further kept stirring for 48 h. Afterwards, the Co-ZIF-8 precursors were obtained by centrifugation and drying. To prepare the Co-SAs/NC, the above Co-ZIF-8 precursors were annealed at 800 °C for 2 h under N_2 atmosphere.

2.2 Synthesis of NC

The NC was prepared with the same procedure of Co-SAs/NC without using of $Co(NO_3)_2 \cdot 6H_2O$.

2.3 Characterizations

The details of electron microscope measurements, N_2 adsorption, X-ray diffraction, X-ray spectroscopy, Raman, and X-ray absorption near edge structure (XANES) measurements were presented in Supporting Information.

2.4 Electrochemical Measurements

The details of ORR measurements were provided in

Supporting Information.

3. Results and Discussion

The overall synthetic process of carbonaceous catalysts with atomically dispersed and nitrogen-coordinated single-atom Co sites (Co-SAs/NC) was operated by a two-step method (**Figure 1a**). Briefly, the Co-ZIF-8 precursors were first assembled via a host-guest confined strategy, wherein the Co species as guest components were confined in the host frameworks of ZIF-8. Subsequently, the Co-SAs/NC was formed by pyrolysis of the as-obtained Co-ZIF-8 precursors at 800 °C. During the pyrolysis process, the Zn species were volatilized and simultaneously ZIF-8 frameworks were carbonized into N-doped carbon skeleton, and the confined Co was in-situ stabilized by the N species in N-doped carbon to formation of the atomically dispersed Co-Nx moiety. However, when the amount of Co was increased in precursor, the metallic Co was observed after the final pyrolysis step (**Figure S1**), indicating that the formation of Co-SAs/NC crucially depends on the amount of the confined Co in precursor.

Moreover, the microstructure of Co-SAs/NC was observed in transmission electron microscopy (TEM) images. Co-SAs/NC displayed an irregular block architecture (**Figures 1b and 1c**), and no nanoparticles were observed in high-magnification TEM image (**Figure 1d**), revealing the Co species was atomically dispersed into the carbonaceous skeleton rather than formation of individual metallic Co or Co-based compounds. Moreover, the atomically dispersed Co species into carbon architecture was further investigated by the advanced aberration-corrected high-angle annular dark field scanning TEM (HAADF-STEM). Clearly, numerous bright dots, corresponding to a high density of Co atoms (Co is heavier than that of C and N), were uniformly distributed across/within the carbon skeleton (**Figures 1e and 1f**). Additionally, the energy-dispersive X-ray spectroscopy mapping images further confirm the presence of Co, C, and N elements in Co-SAs/NC, and all of them were homogeneous distributed across the overall architecture (**Figure 1g**). As a contrast, the NC (**Figure S2**) counterpart could be also controllably assembled by employing the ZIF-8 precursors.

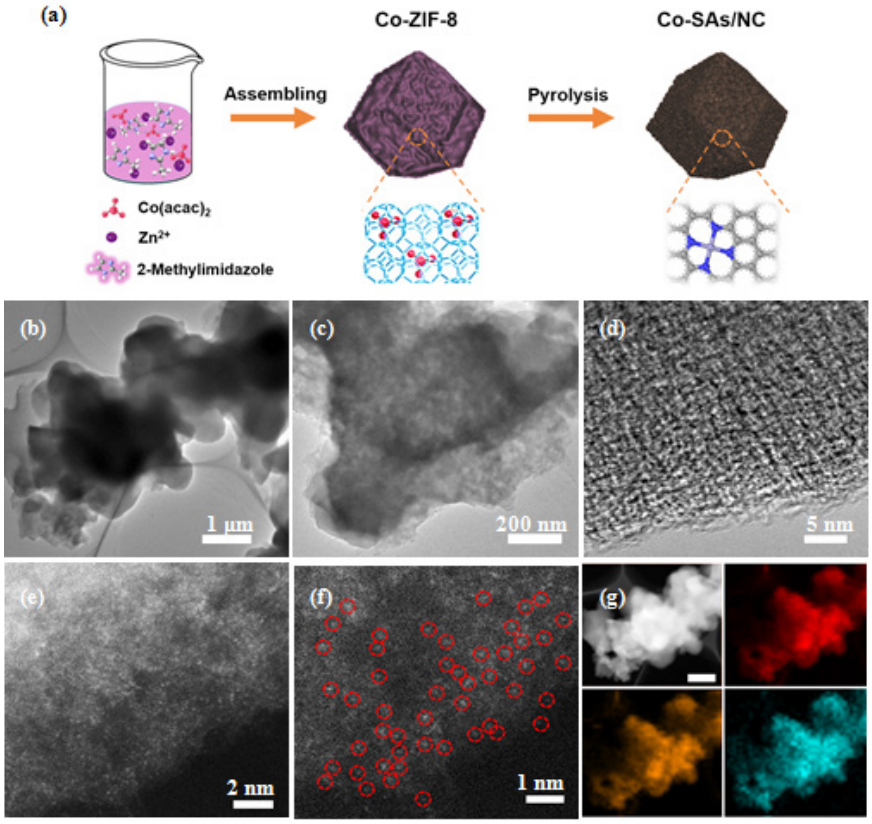

Figure 1. (a) Schematic representation of the synthetic procedure for Co-SAs/NC; (b-d) TEM images; (e,f) aberration-corrected (AC)-HAADF-STEM images of Co-SAs/NC; (g) The corresponding elemental mappings of Co-SAs/NC (scale bar, 1μm)

Moreover, a fast rise of sorption capacity in the low pressure area and an H4 type hysteresis loop were observed in the nitrogen adsorption isotherms of Co-SAs/NC (**Figure 2a**), which reveals that the Co-SAs/NC hold the hierarchical micro-meso-pores[24]. Correspondingly, the pore size distribution curve indicated that the sizes of the pores center mainly at below 4 nm (**Figure 2b**), agreeing well with the observed result in TEM image. The novel porous character of Co-SAs/NC enabled it with a large Brunauer-Emmett-Teller surface area of 794.1 $m^2 \cdot g^{-1}$. Furthermore, X-ray diffraction (XRD) pattern revealed that there are two peaks at 25° and 43.5° in Co-SAs/NC curve, which can be assigned to the characteristic (002) and (101) planes for graphitic carbon (**Figure 2c**), and no additional diffraction peaks of Co-based compounds can be identified, suggesting that the Co species were atomically dispersed in carbon substrate with a long-range disordered character. Moreover, two typical peaks at ~1347 cm^{-1} and 1581 cm^{-1} were observed in the Raman patterns (**Figure S3**), which could be assigned to the D and G bands of carbon. And, the D band and G band were related to the structural defects and degree of graphitization, respectively. Clearly, the Co-SAs/NC displayed a relative strong peak of G-band in comparison with that of NC, revealing the Co species Co-SAs/NC could increase the graphitization degree of its carbonaceous substrate.

The composition and chemical state of Co-SAs/NC were investigated by X-ray photoelectron spectroscopy (XPS). In high-resolution Co 2p spectrum of Co-SAs/NC (**Figure 2d**), the four fitted peaks at 780.8/796.5 eV and 785.2/802.3 eV can be assigned to Co-N as well as the corresponding satellite signals, respectively[25,26]. And, the Co loading in Co-SAs/NC is around 0.89 at.% (determined by XPS) and 1.27 wt% (by inductively coupled plasma optical emission spectrometry, ICP-OES), respectively. And, the N 1s XPS of Co-SAs/NC could be divided into three peaks, which located at 397.9 eV, 399.1 eV, and 400.2 eV for pyridinic N, Co-N species, and pyrrolic N, respectively (**Figure 2e**) [27,28]. Additionally, the C 1s XPS spectra could be fitted into three peaks at binding energies of 284.6 eV, 286.1 eV, and 288.4 eV (**Figure 2f**), which can be assigned to C-C, C-N, and C-O bonds, respectively[29]. The above results further revealed that Co atoms in Co-SAs/NC are anchored by N species in carbon matrix to formation of Co-Nx configuration.

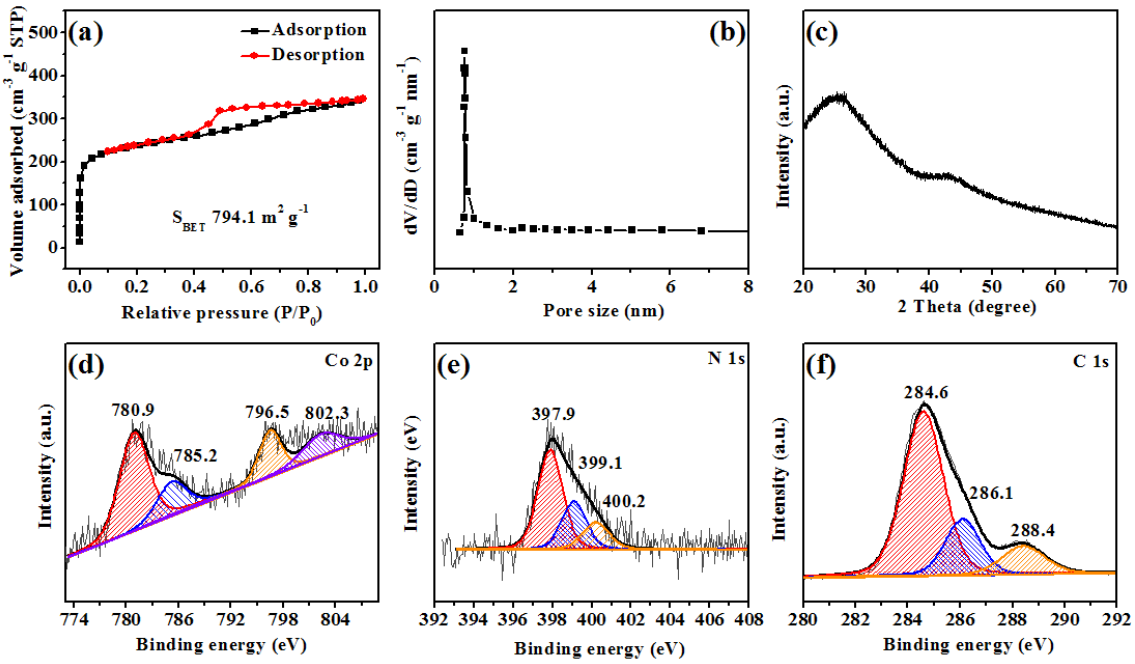

Figure 2. (a) N_2 adsorption-desorption isotherms; (b) corresponded pore-size distribution of Co-SAs/NC; (c) XRD pattern, and high-resolution; (d) Co 2p XPS spectra; (e) N 1s XPS spectra; (f) C 1s XPS spectra of Co-SAs/NC

Moreover, the local atomic coordination of Co species in Co-SAs/NC was further investigated by X-ray absorption fine-structure (XAFS) measurements, and CoO, Co_3O_4, and Co foil were employed as

references. Clearly, the Co K-edge X-ray absorption near-edge structure (XANES) spectra (**Figure 3a**) displayed that the absorption edge positions of Co-SAs/NC is located between Co foil and Co_3O_4, and is amazingly close to that of CoO reference, indicating the Co species in Co-SAs/NC was probability covalently bonded with N to afford a divalent valence state. Furthermore, the corresponding R space (**Figure 3b**) derived from Fe k^3-weighted Fourier transform (FT) displayed the bond length and atomic coordination of Co species. The curve of Co-SAs/NC displayed a typical peak at ~1.51 Å, which could be attributed to Co-N bond in the first shell[30], and no Co-Co signal at ~2.20 Å and Co-O signals were detected, revealing the Co atoms in Co-SAs/NC were atomically dispersed and stabilized by N atoms to formation of the Co-N bond. Additionally, wavelet transform (WT) of Co K-edge EXAFS oscillations was also applied to investigate the backscattering atoms and obtain powerful resolutions in both R-space and k-space[31]. The WT contour plots of Co species in Co-SAs/NC displayed only one intensity maximum, which was assigned to Co-N (6.0 $Å^{-1}$) contribution (**Figure 3c**). Taking all these results together, well-defined architectures of atomically dispersed Co-N_x centers of Co-SAs/NC was successfully constructed.

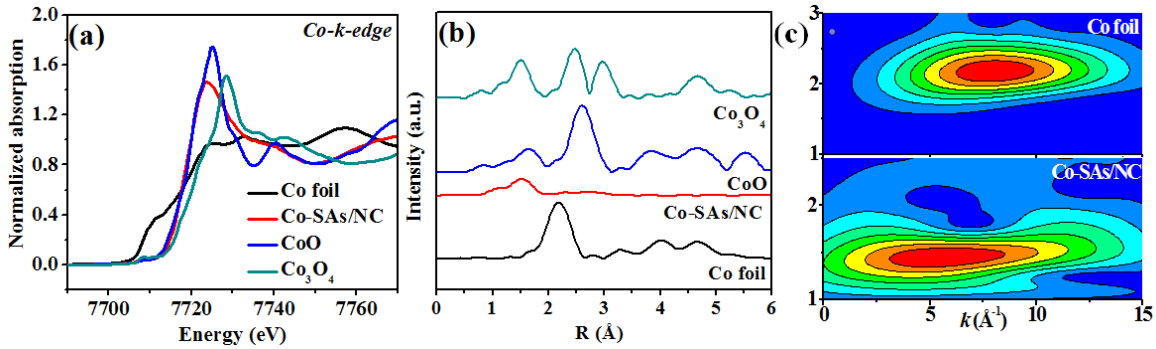

Figure 3. (a) Co K-edge XANES spectra; (b) corresponding Fourier-transformed k^3-weighted EXAFS spectra of Co-SAs/NC, and references of CoO, Co_3O_4, and Co foil; (c) Co K-edge WT-EXAFS contour plots for Co foil and Co-SAs/NC

The ORR performance of Co-SAs/NC was first investigated in O_2-saturated 0.1 M KOH solution, wherein the NC and commercial 20 wt% Pt/C were employed as counterparts for comparison. In the cyclic voltammetry (CV) results, Co-SAs/NC showed a typical reduction peak at the potential of 0.88 V (**Figure 4a**), which is more positive than that of NC (0.80 V) and closed to commercial Pt/C (0.90 V), manifesting the Co single atom anchored by N-doped carbon has a significant impact on the ORR activity. Moreover, the linear sweep voltammograms (LSV) measurement was further employed to evaluate the ORR activity and kinetics. Obviously, the LSV curve of Co-SAs/NC presented the much more positive onset potential (E_{onset}) of 1.01 V than NC (**Figure 4b**), revealing an easier ORR initiation process on Co-SAs/NC. And, Co-SAs/NC also demonstrated an outstanding half-wave potential ($E_{1/2}$, 0.87 V) and a large kinetic current density (J_k, 5.2 mA • cm^{-2}) (**Figure 4c**), which are amazingly superior to those of commercial Pt/C ($E_{1/2}$, 0.86 V, J_k, 3.1 mA • cm^{-2}) as well as NC ($E_{1/2}$, 0.79 V, J_k, 0.5 mA • cm^{-2}) (**Figure 4c**). Moreover, the half-wave potential of Co-SAs/NC was also superior to some of the currently reported results (**Table S1**). Interestingly, Co-SAs/NC also showed an obvious improved ORR activity in term of an outstanding $E_{1/2}$ and large J_k compared to NC catalyst, indicating that the atomically dispersed Co-N_x centers of Co-SAs/NC can greatly improve its ORR activity in comparison with that of N species in NC counterpart. Generally, the ORR mechanism undergoes the multiple proton-coupled electron transfer steps accompanying with complex reaction intermediates (OO*, OOH*, O*, and OH*). Therefore, the efficient strategy to improve the ORR activity and kinetics of the catalyst is to break down the corresponding reaction barrier. Compared with the N-doped carbon, the excellent ORR performances of Co-SAs/NC may be benefited from its Co-Nx moiety, wherein the Co electronic structural characteristics (e.g. d-band center, electron spin) could be regulated by N ligands to effectively optimize the reaction barrier and ORR activity/

kinetics[32,33]. Moreover, Co-SAs/NC also hold a larger electrochemical active surface area (ECSA) than that of bare NC (**Figure S4**), which is also conducive to the improvement of ORR activity.

Apart from the excellent activity and rapid kinetic, the ORR catalytic selectivity and stability of Co-SAs/NC are also the key parameters for its practical application. The rotating disk electrode (RDE) tests at different rotating rates (400 rpm to 2025 rpm) were firstly performed to assess the ORR pathway of series catalysts, the current densities increase with the rotating rates (**Figure 4d, Figures S5 and S6**), indicating the corresponding ORR process is an obviously kinetic controlled process[34]. Moreover, the Koutecky-Levich (K-L) plots derived from LSV curves (**Figure 4e**) further confirmed that the electron transfer number (*n*) of Co-SAs/NC is 3.96, which indicates a near 4e- reduction of O_2 to H_2O pathway as well as agrees well with reported 4e- mechanism[21]. The *n* values of Co-SAs/NC are slightly larger than that of NC (3.87), revealing Co-SAs/NC possesses a higher ORR selectivity. In addition, the methanol crossover test of Co-SAs/NC was also performed. After injection of methanol into the KOH electrolyte, the current density of Co-SAs/NC had only a slight oscillation, but the current density of Pt/C dropped sharply (**Figure S7**), revealing Co-SAs/NC has an excellent methanol tolerance. More importantly, the long-term durability test and corresponding structural characterizations of Co-SAs/NC were operated to evaluate its ORR lifespan. Clearly, the LSV plots of Co-SAs/NC before and after 8000 continuous cycles were almost overlapped (**Figure 4f**), further revealing the excellent stability of Co-SAs/NC. Meanwhile, the component and structural characters of Fe-DAs/NC after ORR (Fe-DAs/NC-spent) were also fully analysized, and all the results of XRD and TEM image revealed its robust structural features (**Figures S8 and S9**).

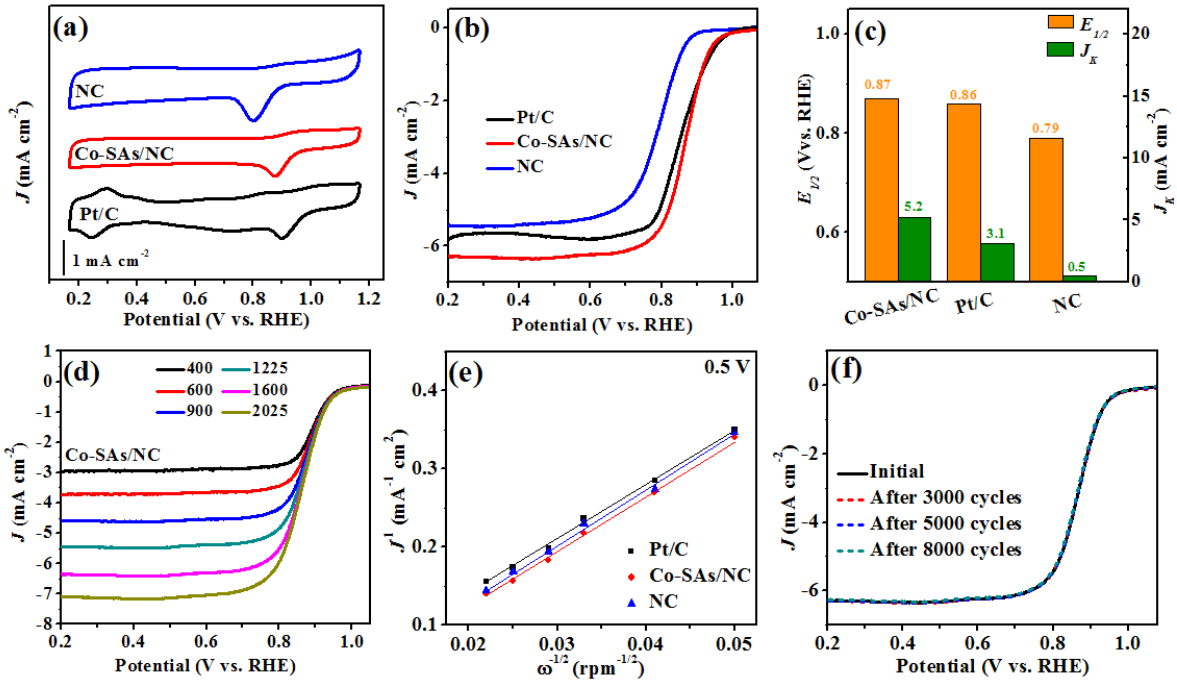

Figure 4. (a) CV curves; (b) LSV curves; (c) summarized half-wave potentials and kinetic current density (at 0.87 V *vs*. RHE) of Co-SAs/NC, NC, and commercial Pt/C; (d) LSV curves of Co-SAs/NC at various rotating rates; (e) K–L plots of Co-SAs/NC, NC, and commercial Pt/C obtained from the RDE data at 0.5 V; (f) LSV curves of Co-SAs/NC before and after 8,000 potential cycles

As the designed Co-SAs/NC displayed excellent ORR performance, a proof-of-concept rechargeable Zn-air battery (ZAB) with Co-SAs/NC as cathode was assembled to deeply evaluate its potential applications. Clearly, all of the Co-SAs/NC, NC, and Pt/C-based ZAB devices can smoothly discharge, and deliver appreciable current densities of 151.5 mA • cm^{-2}, 7.3 mA • cm^{-2} and 50.1 mA • cm^{-2} at cell voltage of 1.0

V, respectively (**Figure 5a**). Moreover, the maximum power density for Co-SAs/NC-based ZAB device is 233.6 mW • cm^{-2} (**Figure 5a**), outperforming 137.3 mW • cm^{-2} of Pt/C-based and 80.5 mW • cm^{-2} of NC-assembled ZAB. Moreover, ZAB with Co-SAs/NC as air cathode displayed a specific capacity of 788.4 mAh • g_{Zn}^{-1} along with a 95.5% utilization of the theoretical capacity (at 10 mA • cm^{-2}), superior to the Pt/C-based ZAB (741.7 mAh • g^{-1}) and NC-based ZAB (625.1 mAh • g^{-1}) (**Figure 5b**)[35]. In addition, Co-SAs/NC-based ZAB device, operated at 10 mA • cm^{-2} with a 10 min per cycle period, also showed an excellent long-life cycling performance (**Figure 5c**). In the initial cycle, the typical discharge and charge voltages for this ZAB are 1.20 V and 2.28 V, respectively, corresponding to a 1.08 V voltage gap and a high trip efficiency of 52.6%. Amazingly, negligible voltage fading was observed for Co-SAs/NC-based ZAB even within at least 1000 cycles, whereas both of the Pt/C-based ZAB and NC-based ZAB devices showed an obvious enlarged voltage gap with the increasing cycles, respectively, revealing the excellent stability of Co-SAs/NC in practical ZAB device.

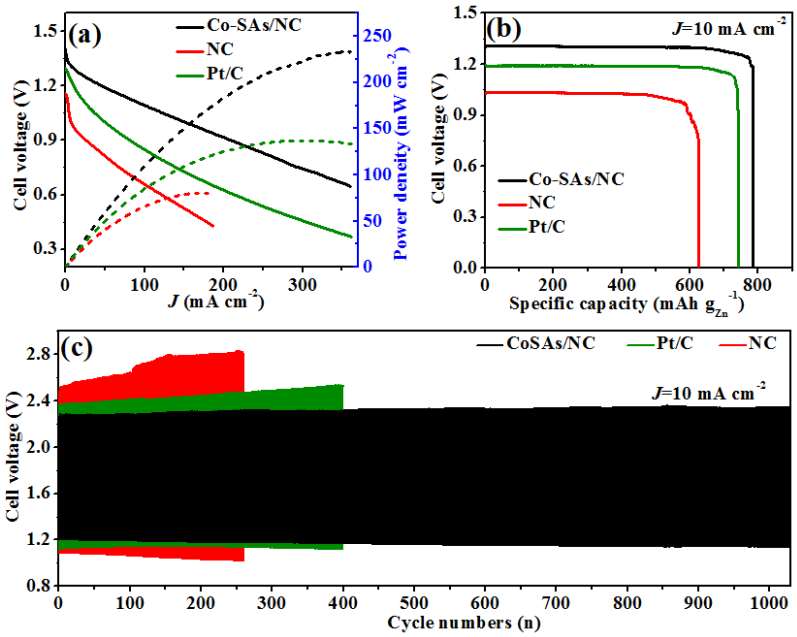

Figure 5. (a) Discharge curves along with corresponding power densities; (b) Voltage-capacity curves; (c) galvanostatic discharge/charge plots of home-made zinc-air battery (ZAB) based on Co-SAs/NC, NC and commercial Pt/C

4. Conclusions

In summary, the Co-SAs/NC was successfully synthesized by pyrolysis of nano-confined Co-precursors. And, the atomic configurations and electronic structures of Co-SAs/NC were investigated by detailed characterizations of HAADF-STEM and XAS techniques. Co-SAs/NC exhibited excellent ORR performance in alkaline electrolyte with a large onset and half-wave potentials of 1.01 V and 0.87 V, respectively, as well as good selectivity and favorable stability. Moreover, Zn-air battery assembled with Co-SAs/NC showed excellent performances in specific capacity, power density, and stability, which indicated that the Co-SAs/NC has promising potential for practical applications.

Acknowledgements

This work was supported by the Natural Science Foundation of Hebei Province (B2020204017 and B2022204001) and the Scientific Research Foundation of Hebei Agricultural University (YJ201932).

Conflict of Interest

The authors declare that they have no known competing financial interests or personal relationships that could influence the work reported in this paper.

References

[1] Pan J, Xu YY, Yang H, *et al*. Advanced architectures and relatives of air electrodes in Zn-air batteries.

Advanced Science, 2018;5(4):1700691.
https://doi.org/10.1002/advs.201700691

[2] He T, Chen Y, Liu Q, *et al*. Theory-guided regulation of FeN4 spin state by neighboring Cu atoms for enhanced oxygen reduction electrocatalysis in flexible metal-air batteries. *Angewandte Chemie International Edition*, 2022;61(27):e202201007.
https://doi.org/10.1002/anie.202201007

[3] Li Y, Cui M, Yin Z, *et al*. Metal-organic framework based bifunctional oxygen electrocatalysts for rechargeable zinc-air batteries: current progress and prospects. *Chemical Science*, 2020;11(43):11646-11671.
https://doi.org/10.1039/D0SC04684A

[4] Lin X, Shi L, Liu F, *et al*. Large-scale production of holey carbon nanosheets implanted with atomically dispersed Fe sites for boosting oxygen reduction electrocatalysis. *Nano Research*, 2022;15:1926-1933.
https://doi.org/10.1007/s12274-021-3816-y

[5] Yu P, Wang L, Sun F, *et al*. Co Nanoislands rooted on Co-N-C nanosheets as efficient oxygen electrocatalyst for Zn-air batteries. *Advanced Materials*, 2019;31(30):1901666.
https://doi.org/10.1002/adma.201901666

[6] Holby EF, Wang G and Zelenay P. Acid stability and demetalation of PGM-free ORR electrocatalyst structures from density functional theory: a model for "single-atom catalyst" dissolution. *ACS Catalysis*, 2020;10:14527-14539.
https://doi.org/10.1021/acscatal.0c02856

[7] Liu M, Zhao Z, Duan X, *et al*. Nanoscale structure design for high-performance Pt-based ORR catalysts. *Advanced Materials*, 2019;31(6):1802234.
https://doi.org/10.1002/adma.201802234

[8] Wu ZP, Lu XF, Zang SQ, *et al*. Non-noble-metal-based electrocatalysts toward the oxygen evolution reaction. *Advanced Functional Materials*, 2020;30(15):1910274.
https://doi.org/10.1002/adfm.201910274

[9] Hu C and Dai L. Carbon-based metal-free catalysts for electrocatalysis beyond the ORR. *Angewandte Chemie International Edition*, 2016;55(39):11736-11758.
https://doi.org/10.1002/anie.201509982

[10] Greeley J, Stephens IEL, Bondarenko AS, *et al*. Alloys of platinum and early transition metals as oxygen reduction electrocatalysts. *Nature Chemistry*, 2009;1(7):552-556.
https://doi.org/10.1038/nchem.367

[11] Chen Z, Higgins D, Yu A, *et al*. A review on non-precious metal electrocatalysts for PEM fuel cells. *Energy & Environmental Science*, 2011;4(9):3167-3192.
https://doi.org/10.1039/C0EE00558D

[12] Artyushkova K, Matanovic I, Halevi B, *et al*. Oxygen binding to active sites of Fe-N-C ORR electrocatalysts observed by ambient-pressure XPS. *The Journal of Physical Chemistry C*, 2017;121(5):2836-2843.
https://doi.org/10.1021/acs.jpcc.6b11721

[13] Wang R, Zhang P, Wang Y, *et al*. ZIF-derived Co-N-C ORR catalyst with high performance in proton exchange membrane fuel cells. *Progress in Natural Science: Materials International*, 2020;30(6):855-860.
https://doi.org/10.1016/j.pnsc.2020.09.010

[14] Wang X, Chen Z, Han Z, *et al*. Manipulation of new married edge-adjacent Fe_2N_5 catalysts and identification of active species for oxygen reduction in wide pH range. *Advanced Functional Materials*, 2022;32(18):2111835.
https://doi.org/10.1002/adfm.202111835

[15] Kong F, Huang Y, Chen M, *et al*. Creation of densely exposed and cavity-edged single Fe active sites for enhanced oxygen electroreduction. *Applied Catalysis B: Environmental*, 2022;317:121768.
https://doi.org/10.1016/j.apcatb.2022.121768

[16] Chen Y, Ji S, Chen C, *et al*. Single-atom catalysts: synthetic strategies and electrochemical applications. *Joule*, 2018;2(7):1242-1264.
https://doi.org/10.1016/j.joule.2018.06.019

[17] Wang A, Li J and Zhang T. Heterogeneous single-atom catalysis. *Nature Reviews Chemistry*, 2018;2(6):65-81.
https://doi.org/10.1038/s41570-018-0010-1

[18] Qiu X, Yan X, Pang H, *et al*. Isolated Fe single atomic sites anchored on highly steady hollow graphene nanospheres as an efficient electrocatalyst for the oxygen reduction reaction. *Advanced Science*, 2019;6(2):1801103.
https://doi.org/10.1002/advs.201801103

[19] Han X, Ling X, Wang Y, *et al*. Generation of nanoparticle, atomic-cluster, and single-atom cobalt catalysts from zeolitic imidazole frameworks by spatial isolation and their use in zinc-air batteries. *Angewandte Chemie*, 2019;131(16):5413-5418. https://doi.org/10.1002/ange.201901109

[20] Chen Y, Gao R, Ji S, *et al*. Atomic-level modulation of electronic density at cobalt single-atom sites derived from metal-organic frameworks: enhanced oxygen reduction performance. *Angewandte Chemie International Edition*, 2021;60(6):3212-3221. https://doi.org/10.1002/anie.202012798

[21] Sun T, Zhao S, Chen W, *et al*. Single-atomic cobalt sites embedded in hierarchically ordered porous nitrogen-doped carbon as a superior bifunctional electrocatalyst. *Proceedings of the National Academy of Sciences*, 2018;115(50):12692-12697. https://doi.org/10.1073/pnas.1813605115

[22] Zang W, Sumboja A, Ma Y, *et al*. Single Co atoms anchored in porous N-doped carbon for efficient zinc-air battery cathodes. *Acs Catalysis*, 2018;8(10):8961-8969. https://doi.org/10.1021/acscatal.8b02556

[23] Zhou L, Zhou P, Zhang Y, *et al*. 3D star-like atypical hybrid MOF derived single-atom catalyst boosts oxygen reduction catalysis. *Journal of Energy Chemistry*, 2021;55:355-360. https://doi.org/10.1016/j.jechem.2020.06.059

[24] Meng T, Qin J, Wang S, *et al*. In situ coupling of Co 0.85 Se and N-doped carbon via one-step selenization of metal-organic frameworks as a trifunctional catalyst for overall water splitting and Zn-air batteries. *Journal of Materials Chemistry A*, 2017;5(15):7001-7014. https://doi.org/10.1039/C7TA01453H

[25] He J, Li N, Li ZG, *et al*. Strategic defect engineering of metal-organic frameworks for optimizing the fabrication of single-atom catalysts. *Advanced Functional Materials*, 2021;31(41):2103597. https://doi.org/10.1002/adfm.202103597

[26] Feng J, Tang R, Liu G, *et al.* Regulating d-orbital electronic character and HER free energy of VN electrocatalyst by anchoring single atom. *Chemical Engineering Journal*, 2023;452:139131. https://doi.org/10.1016/j.cej.2022.139131

[27] Zhou B, Liu Y, Wu X, *et al*. Wood-derived integrated air electrode with Co-N sites for rechargeable zinc-air batteries. *Nano Research*, 2022;15(2):1415-1423. https://doi.org/10.1007/s12274-021-3678-3

[28] Cheng Q, Han S, Mao K, *et al*. Co nanoparticle embedded in atomically-dispersed Co-NC nanofibers for oxygen reduction with high activity and remarkable durability. *Nano Energy*, 2018;52:485-493. https://doi.org/10.1016/j.nanoen.2018.08.005

[29] Wang Y, Tao L, Xiao Z, *et al*. 3d carbon electrocatalysts in situ constructed by defect-rich nanosheets and polyhedrons from NaCl-sealed zeolitic imidazolate frameworks. *Advanced Functional Materials*, 2018;28(11):1705356. https://doi.org/10.1002/adfm.201705356

[30] Yuan E, Zhou M, Shi G, *et al*. Ultralow-loading single-atom cobalt on graphitic carbon nitrogen with robust Co-N pairs for aerobic cyclohexane oxidation. *Nano Research*, 2022;15(10):8791-8803. https://doi.org/10.1007/s12274-022-4556-3

[31] Wang Z, Jin X, Zhu C, *et al*. Atomically dispersed Co_2-N_6 and Fe-N_4 costructures boost oxygen reduction reaction in both alkaline and acidic media. *Advanced Materials*, 2021;33(49):2104718. https://doi.org/10.1002/adma.202104718

[32] Zhu X, Tan X, Wu KH, *et al*. Intrinsic ORR activity enhancement of Pt atomic sites by engineering the d-band center via local coordination tuning. *Angewandte Chemie International Edition*, 2021;60(40):21911-21917. https://doi.org/10.1002/anie.202107790

[33] Zhong W, Qiu Y, Shen H, *et al*. Electronic spin moment as a catalytic descriptor for Fe single-atom catalysts supported on C_2N. *Journal of the American Chemical Society*, 2021;143(11):4405-4413. https://doi.org/10.1021/jacs.1c00889

[34] Chai L, Hu Z, Wang X, *et al*. Fe_7C_3 nanoparticles with in situ grown CNT on nitrogen doped hollow carbon cube with greatly enhanced conductivity and ORR performance for alkaline fuel cell. *Carbon*, 2021;174:531-539. https://doi.org/10.1016/j.carbon.2020.12.070

[35] Feng J, Tang R, Wang X, *et al*. Biomass-derived activated carbon sheets with tunable

oxygen functional groups and pore volume for high-performance oxygen reduction and Zn-air batteries. *ACS Applied Energy Materials*, 2021;4(5):5230-5236. https://doi.org/10.1021/acsaem.1c00755

Supplementary Information

1. Experimental

1.1 Characterizations

The microstructures of the as-obtained products was observed on the transmission electron microscopy [TEM, JEOL JEM-2010], and high-angle annular dark field-scanning transmission electron microscopy [HAADF-STEM, JEOL ARM200F], respectively. N_2 adsorption-desorption isotherms were tested using a Belsorp-max sorption analyzer at liquid nitrogen temperature (77 K). The phase was detected by X-ray diffraction (XRD) (Bruker D8, Cu-Kα radiation). X-ray spectroscopy (XPS) was performed on an ESCALAB 250 spectrometer (Perkin-Elmer). Raman spectra were collected on an Invia Raman spectrometer with the excitation laser wavelength of 633 nm. X-ray absorption near edge structure (XANES) measurements were undertaken at the Beamlines 1W1B in Beijing Synchrotron Radiation Facility (BSRF).

1.2 ORR

The slurry was prepared by dispersing of 4 mg of catalyst in 1 mL of solvent, which containing of 900 μL ethylalcohol and 100 μL 0.5 wt% Nafion aqueous solution. Then, 20 μL of the as-prepared slurry was dropped on a polished glass carbon electrode (diameter 5 mm) and dried naturally.

The ORR measurement was investigated in O_2-saturated 0.1 M KOH electrolyte with a three-electrode mode, where in the rotating ring disk (RRDE) with catalyst as the working electrode, Ag/AgCl (3 M KCl) as a reference electrode, graphite rod as a counter electrode, respectively. The CV and LSV were obtained at ambient temperature after purging O_2 or N_2 gas for 30 min with a scan rate of 10 mV • s^{-1}. All the measured potentials were normalized to a RHE electrode.

RDE measurements were carried out at rotating rates varying from 400 rpm to 2025 rpm at a scan rate of 10 mV • s^{-1}. The kinetic parameters can be obtained on the basis of Koutecky-Levich equations as follows:

$$1/J = 1/J_k + 1/(B\omega^{1/2}) \quad (1)$$

$$B = 0.2nFC_oD_o^{2/3}\upsilon^{-1/6} \quad (2)$$

$$J_k = nFkC_o \quad (3)$$

Where J is the measured current density, J_k is the kinetic current densities, ω is the rotation speed (the constant 0.2 is used when the rotation speed is expressed in rpm), n is the transferred electron number, F is the Faraday constant (96,485 C • mol^{-1}), C_o is the saturated concentration of O_2 in the electrolyte (1.21×10^{-3} mol • L^{-1}), D_o is the diffusion coefficient of O_2 in the solution (1.9×10^{-5} cm • s^{-1}), υ is the kinetic viscosity of the electrolyte (0.01 cm^2 • s^{-1}), and k is the electron-transfer rate constant.

1.3 Zn-air battery

The rechargeable Zn-air batteries were tested in home-made electrochemical cells, and the synthesized Co-SAs/NC was coated on substrate of carbon paper as the air cathodes, a polished Zn plate was applied as the anode, and a 6 M KOH aqueous solution was utilized as the electrolyte. Battery testing was performed at room temperature on a LAND CT2001A instrument. For the cycling tests, one cycle consisted of one discharging step (10 mA • cm^{-2} for 5 min) followed by one charging step of the same current density and duration time.

2. Supplementary Figures

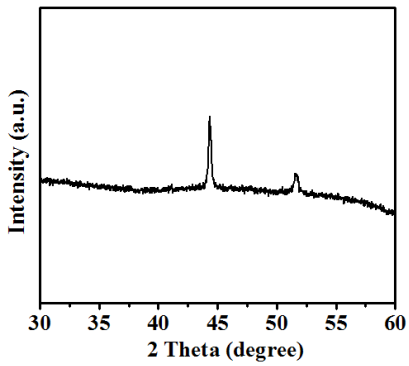

Figure S1. XRD pattern of metallic Co/NC

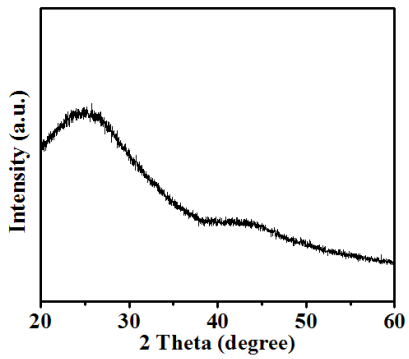

Figure S2. XRD pattern of NC

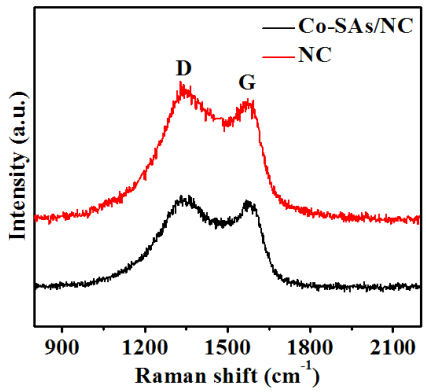

Figure S3. Raman patterns of Co-SAs/NC and NC

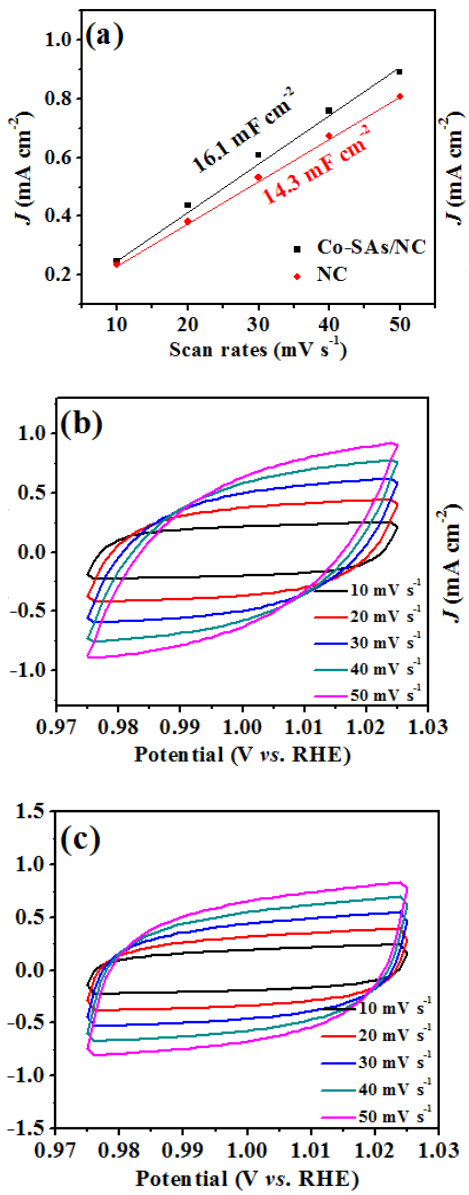

Figure S4. (a) Plots of the current density vs the scan rate for Co-SAs/NC and NC. Cyclic voltammograms (CVs) for (b) Co-SAs/NC and (c) NC

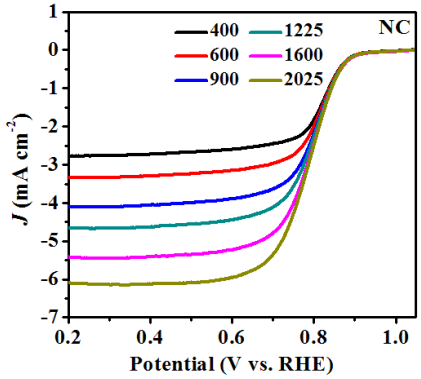

Figure S5. LSV curves of NC at various rotating rates

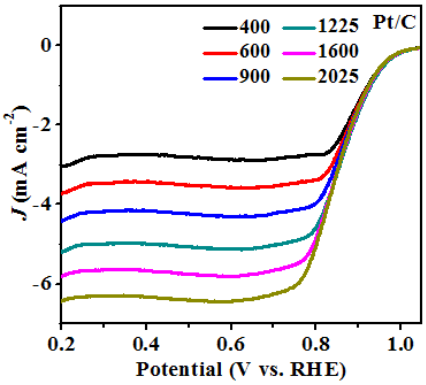

Figure S6. LSV curves of Pt/C at various rotating rates

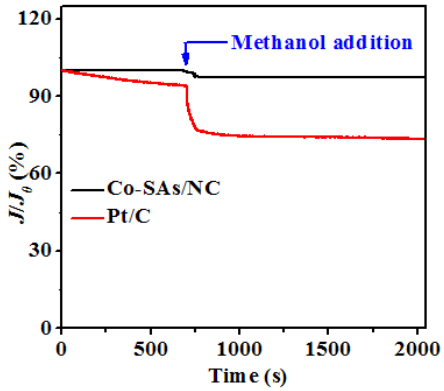

Figure S7. Methanol tolerance tests of Co-SAs/NC and Pt/C

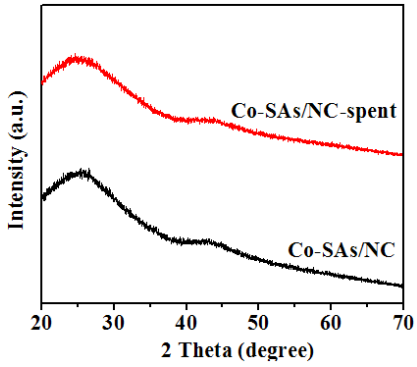

Figure S8. XRD pattern of Co-SAs/NC before and after ORR test

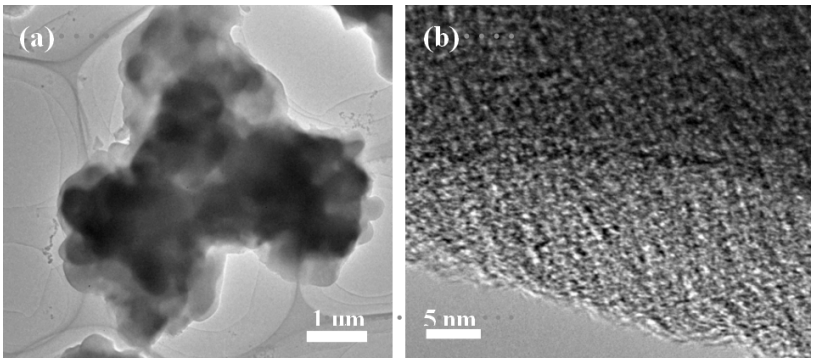

Figure S9. TEM images of Co-SAs/NC before and after ORR test

3. Supplementary Table

Table S1. The ORR activity comparison of Co-SAs/NC with non-noble metal-based catalysts previously reported in 0.1 M KOH solution

Catalyst	Loading (mg·cm^{-2})	E_{onset} (V)	$E_{1/2}$ (V)	Supplementary Ref.
Co-SAs/NC	0.2	1.01	0.87	This work
CoNi-SAs/NC	0.4	0.88	0.76	[1]
Co-N,B-CSs	0.1	0.89	0.83	[2]
Fe-ACSA@NC	0.26	1.03	0.9	[3]
Co@MCM	0.51	0.95	0.86	[4]
OLC/Co-N-C	0.2	/	0.855	[5]
Zn/CoN-C	0.255	1.004	0.861	[6]
Fe3C-Co/NC	0.2	0.94	0.885	[7]
CoFe/N-GCT	5.97	0.88	0.76	[8]
CoFe/SNC-25	0.354	/	0.843	[9]
CoNi@NCNT	0.408	0.97	0.87	[10]
Co-Fe/NC-700	0.25	/	0.854	[11]
Fe1Co1-CNF	~0.2	0.99	0.87	[12]
FeAB-O	0.2	/	0.9	[13]

Supplementary References

[1] Han X, Ling X, Yu D, *et al*. Atomically dispersed binary Co-Ni sites in nitrogen-doped hollow carbon nanocubes for reversible oxygen reduction and evolution. *Advanced Materials*, 2019;31(49):1905622. https://doi.org/10.1002/adma.201905622

[2] Guo Y, Yuan P, Zhang J, *et al*. Carbon nanosheets containing discrete Co-Nx-By-C active sites for efficient oxygen electrocatalysis and rechargeable Zn-air batteries. *ACS Nano*, 2018;12(2):1894-1901. https://doi.org/10.1021/acsnano.7b08721

[3] Huang H, Yu D, Hu F, *et al*. Clusters induced electron redistribution to tune oxygen reduction activity of transition metal single-atom for metal-air batteries. *Angewandte Chemie*, 2022;134(12):e202116068. https://doi.org/10.1002/ange.202116068

[4] Zhang H, Zhou W, Chen T, *et al*. A modular strategy for decorating isolated cobalt atoms into multichannel carbon matrix for electrocatalytic oxygen reduction. *Energy & Environmental Science*, 2018;11(8):1980-1984. https://doi.org/10.1039/C8EE00901E

[5] Liang Z, Kong N, Yang C, *et al*. Highly curved nanostructure-coated Co, N-doped carbon materials for oxygen electrocatalysis. *Angewandte Chemie International Edition*, 2021;60(23):12759-12764. https://doi.org/10.1002/ange.202101562

[6] Lu Z, Wang B, Hu Y, *et al*. An isolated zinc-

cobalt atomic pair for highly active and durable oxygen reduction. *Angewandte Chemie*, 2019;131(9):2648-2652. https://doi.org/10.1002/ange.201810175

[7] Yang CC, Zai SF, Zhou YT, *et al*. Fe_3C-Co nanoparticles encapsulated in a hierarchical structure of N-doped carbon as a multifunctional electrocatalyst for ORR, OER, and HER. *Advanced Functional Materials*, 2019;29(27):1901949. https://doi.org/10.1002/adfm.201901949

[8] Liu X, Wang L, Yu P, *et al*. A stable bifunctional catalyst for rechargeable zinc-air batteries: iron-cobalt nanoparticles embedded in a nitrogen-doped 3D carbon matrix. *Angewandte Chemie International Edition*, 2018;57(49):16166-16170. https://doi.org/10.1002/anie.201809009

[9] Li C, Zhou E, Yu Z, *et al*. Tailor-made open porous 2D CoFe/SN-carbon with slightly weakened adsorption strength of ORR/OER intermediates as remarkable electrocatalysts toward zinc-air batteries. *Applied Catalysis B: Environmental*, 2020;269:118771. https://doi.org/10.1016/j.apcatb.2020.118771

[10] Niu W, Pakhira S, Marcus K, *et al*. Apically dominant mechanism for improving catalytic activities of N-doped carbon nanotube arrays in rechargeable zinc–air battery. *Advanced Energy Materials*, 2018;8(20):1800480. https://doi.org/10.1002/aenm.201800480

[11] Zhang SL, Guan BY and Lou XW. Co-Fe alloy/N-doped carbon hollow spheres derived from dual metal-organic frameworks for enhanced electrocatalytic oxygen reduction. *Small*, 2019;15(13):1805324. https://doi.org/10.1002/smll.201805324

[12] Wang Y, Li Z, Zhang P, *et al*. Flexible carbon nanofiber film with diatomic Fe-Co sites for efficient oxygen reduction and evolution reactions in wearable zinc-air batteries. *Nano Energy*, 2021;87:106147. https://doi.org/10.1016/j.nanoen.2021.106147

[13] Chen K, Liu K, An P, *et al*. Iron phthalocyanine with coordination induced electronic localization to boost oxygen reduction reaction. *Nature Communications*, 2020;11(1):4173. https://doi.org/10.1038/s41467-020-18062-y